SCIENTIFIC REPORTS
nature research

Check for updates

OPEN

Ultra-compact and high-performance polarization beam splitter assisted by slotted waveguide subwavelength gratings

Chia-Chih Huang[1] & Chia-Chien Huang[2]✉

We propose an ultra-short polarization beam splitter (PBS) consisting of two slot waveguides assisted by slotted waveguide subwavelength gratings (SWSWGs), located between the two slotted waveguides. By controlling the optical momentum of evanescent waves with the anisotropic characteristics of the SWSWGs, we considerably suppress and enhance the couplings of transverse-electric (TE) and transverse-magnetic (TM) modes, respectively, concurrently improving performances and reducing length of the proposed PBS, compared with conventional slotted waveguide couplers (CSWCs). Exceptionally, a transition point is found to show almost zero crosstalk between waveguides for the TE mode, i.e., infinite coupling length. Differing from conventional single-material SWGs, the SWSWGs not only simplify the fabrication process but improve polarization extinction ratio (PER). Numerical results demonstrate the improvement in PER_{TM} (PER_{TE}) from approximately 13 (23) dB for the CSWCs to 26 (24) dB for the present structure, with a > 70% reduction in device length, operating at the wavelength of λ = 1,550 nm. Our design achieves performance of PER_{TM} > 25 dB and PER_{TE} > 20 dB, and insertion loss (IL) < 0.05 dB for TE and < 0.3 dB for TM modes within a bandwidth width (BW) of ~ 50 nm from λ = 1,530 to 1,580 nm. Additionally, geometry deviation is also investigated to assess experimental tolerance. The present idea provides an approach for improving PER, device length, and operating BW of PBSs composed of various waveguide couplers.

Combing electronic and photonic devices in photonic integrated circuits (PICs) is essential to progress in high-density integration and nanophotonics. Silicon-on-insulator (SOI) technology is the candidate platform for realizing this long-term goal[1,2] as it offers two main benefits: Mature complementary metal-oxide semiconductor (CMOS)-compatible technology, and high refractive index contrast, enabling more compact devices. Inevitably, the SOI platform causes strong polarization dependence due to its high birefringence, which is detrimental in optical-fiber systems. Therefore, use of polarization-division multiplexing devices including polarization beam splitters (PBSs) and rotators has been reported to deal with the issue[3–5]. The most widely used are PBSs designed to separate two orthogonal polarization states: The transverse-electric (TE) mode the and transverse-magnetic (TM) mode. As a result, PBSs employing different splitting approaches[5,6] have been proposed, such as adiabatic taper waveguides (ATWs)[6], multi-mode interference (MMI)[7,8], waveguide grating couplers[9,10], computationally optimized metamaterials[11], and directional couplers (DC)[12–15]. Generally, there are some criteria including: (1) polarization extinction ratio (PER); (2) insertion loss (IL); (3) operating bandwidth (BW); (4) the device dimension, and (5) fabrication difficulty to evaluate the merits of a PBS. Although the ATW-based PBS[6] of hundreds of micrometers is long due to its gradually evolving geometry, it offers high fabrication error tolerance and broadband operation. MMI-based PBSs[7,8] require a simpler fabrication process due to their use of wide rectangular waveguides but have the drawback of an extremely long structure (> 1,000 μm) unless assisted design is used. Waveguide grating-based PBSs[9,10] can achieve a footprint of tens of micrometers but their complex fabrication and large scattering loss make them be often used in specific condition such as coupling power from one component to another. Recently, researchers have adopted free-form metamaterials to design PBSs with an ultra-small area of $2.4 \times 2.4\ \mu m^2$ using computational optimization[11]. Nevertheless, the time-consuming design

[1]Department of Electronic Engineering, Tungnan University, No. 152, Sec. 3, Beishen Rd., Shenkeng Dist., New Taipei City 222, Taiwan, ROC. [2]Department of Physics and Institute of Nanoscience, National Chung Hsing University, 145, Xingda Rd., Taichung 402, Taiwan, ROC. ✉email: cch@phys.nchu.edu.tw

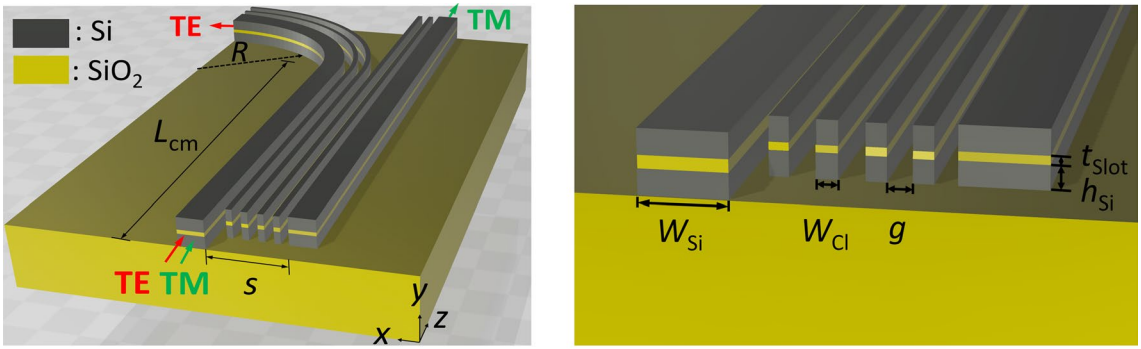

(a) (b)

Figure 1. (**a**) 3D schematic diagram of our designed PBS and (**b**) the zoomed-in view of the input port.

and a low PER of ~ 10 dB with a narrow BW of 32 nm make it unsatisfactory in designing high-performance PBSs. Compared with these mechanisms mentioned above, DC-based PBSs[12–15] are more attractive due to their comparatively small dimensions, acceptable performances, various design approaches, and simpler structures.

For the DC-based PBSs, the phase matching condition (PMC) is satisfied to separate two polarization modes, in which one mode is coupled to the cross channel and the other mode propagating along the through channel is designed to be deviated from the PMC. Hence, DC-based PBSs can be built flexibly by using several possible waveguide structures. In Ref.[12] reported by Fukuda et al., a DC-based PBS with a footprint of $7 \times 16\ \mu m^2$, implemented with a Si-strip coupler on an SOI platform, with calculated PER_{TE} (PER_{TM}) about 15 (10) and IL_{TE} (IL_{TM}) about 0.5 (0.5) dB, in the C-band range. In Ref.[13], Guan et al. proposed an asymmetric DC-based PBS composed a silicon (Si) strip and a hybrid plasmonic waveguide. Within a 120 nm working BW, the footprint of the device is with $1.9 \times 3.7\ \mu m^2$ and their PERs are > 12 dB. Although that device length is extremely short, the PERs of 12 dB require considerable improvement. Instead of adopting two Si strips, Yue et al.[14] used two slot waveguides[16,17] to build a PBS to enhance polarization dependence by effectively increasing TM mode coupling compared with that of Ref.[14]. The device length of Ref.[14] is thus shrunk to 46.7 μm compared with that of 350 μm using two Si strips[12]. However, the calculated PERs of Ref.[14] were around 20 dB within an 18 nm operating BW. Subsequently, Zhang et al.[15] experimentally demonstrated the PERs of 16.8 and 14.1 dB for TE and TM modes, respectively, for the design of Ref.[14].

In principle, subwavelength gratings (SWGs), comprising dielectric strips of much smaller dimension than the working wavelength, which behave as homogeneous media with an equivalent anisotropic refractive index[23] depending on the geometry of the structure and the polarization of the electromagnetic wave propagating within it, alleviating the limited choice of material refractive indices and further enabling the design of high-performance photonic devices. The desired material properties can be controlled by varying the constituent dielectrics, duty cycle, or number of gratings, providing an extra degree of freedom for tailoring the required mode characteristics. Many photonic devices[18–25] designed by adopting SWGs in the waveguides have recently been reported, following the modern fabrication technology. More recently, Jahani and Jacob[26–28] located SWGs in the regions between waveguides to significantly reduce crosstalk. Also, Xu et al.[29] adopted SWGs in both the waveguide and cladding regions to form a hetero-anisotropic slab structure, while the slab performs as an MMI coupler and a two isolated waveguides for the TM and TE polarizations, respectively. Li et al.[30] introduced a pair of cascaded dual-core adiabatic tapers consisting of a tapered SWG and regular adiabatic tapered waveguides to achieve low ILs and high PERs. In the present work, we propose a PBS comprising two main slotted waveguides, assisted by slotted waveguide subwavelength gratings (SWSWGs) located between the two slotted waveguides. By controlling the optical momentum of evanescent waves with the anisotropic SWSWGs, we can not only significantly suppress the crosstalk of TE mode but considerably enhance the coupling strength of TM mode, to substantially improve PER_{TM} and reduce the device length by around a quarter compared with a conventional slotted waveguide coupler (CSWC)[14]. In addition, a transition point showing almost zero crosstalk (i.e., infinite coupling length) of the TE mode is found in the present structure.

Results and discussion

Analysis of mode coupling based on optical momentum of evanescent wave. A 3D schematic of the proposed PBS is shown in Fig. 1a, and the zoomed-in view of the cross section of the input is shown in Fig. 1b. The proposed design comprises two horizontal slotted waveguides with SWSWGs located between the slotted waveguides. The two slotted waveguides and SWSWGs all comprise a low-index SiO_2 slot layer sandwiched between two high-index Si layers. To effectively decouple the two output powers, a 90° angled slotted waveguide with the radius of curvature, R, is connected to a slotted waveguide delivering the TE mode, while another straight slotted waveguide carries the power of the TM mode. Note that an equal number of SWSWGs is distributed between each of the two output ports. The substrate and cladding are SiO_2 and air, respectively.

The relevant parameters are the Si width of the slotted waveguides W_{Si} with edge-to-edge spacing s, the width of the SWSWGs W_{cl}, and the height h_{Si} and thickness t_{slot} of the Si and slot layer. The SWSWG pitch is set to $\Lambda = W_{cl} + g$ and with duty cycle $\rho = W_{cl}/\Lambda$, where g is the gap between the strips. Note that Λ is set under the subwavelength to suppress diffraction effects[23]. The input TM mode with major electric component in the

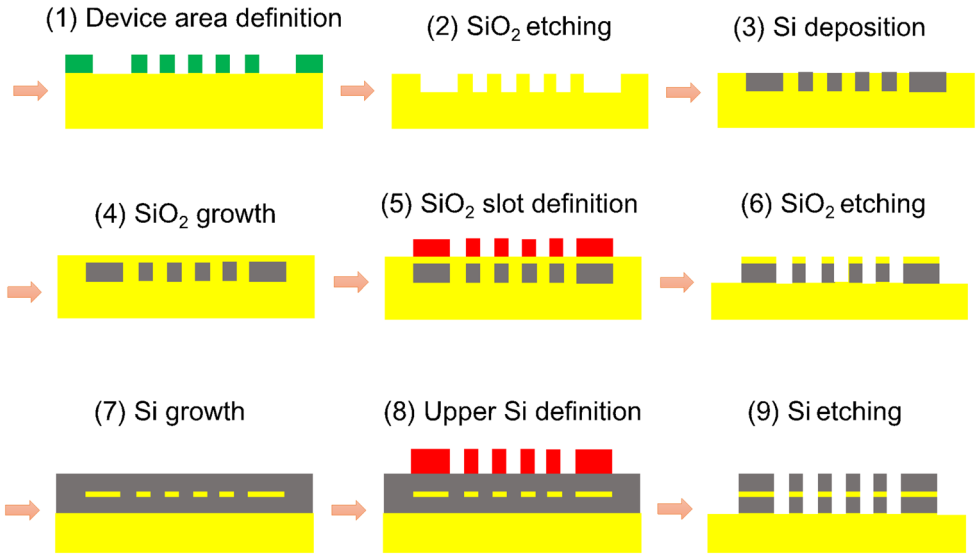

Figure 2. Schematic diagram of the fabrication processes of the present device.

y-direction, E_y, is coupled to the adjacent slotted waveguide with the help of the SWSWGs, while the TE mode with major electric component in the *x*-direction, E_x, is guided along the through bar connected by a curved waveguide with negligible power coupling. The processes required for practical fabrication of the proposed device are shown schematically in Fig. 2. Prior to these processes, the patterned hard masks for the curved TE channel, straight TM channel, and SWSWGs are fabricated using high resolution electron beam lithography. After that, the fabrication processes of the proposed structure are shown below:

(1) Preparing a SiO_2 substrate (yellow) for deposition with a negative photoresist (PR) film (green) of height h_{Si} to pattern the lower Si layer of the proposed PBS with the preceding masks, a PR exposure with ultraviolet (UV) light, development, and an etching process. (2) The pattern of the proposed structure is formed by etching SiO_2 and lifting off the PR film. (3) After depositing a Si layer in the trenches using chemical vapor deposition in the wells, a chemical mechanical polishing (CMP) process is used to attain a flat plane. (4) Similarly, a SiO_2 layer of height t_{slot} is deposited using thermal oxidation, then CMP is used to obtain a flat SiO_2 surface. (5) To define a SiO_2 layer, a positive PR film (red) is deposited on the flat SiO_2 surface. The patterned hard masks are used to pattern the PR film. (6) Before lifting off the PR, reactive ion etching is used to form the SiO_2 slot layer. (7) Depositing a Si layer with the height h_{Si}, and using CMP process to have a flat Si film. (8) The upper Si layer is defined using the same process as (5) except for deposition of a positive PR film on the Si layer. (9) After Si etching, the PR film is removed to obtain the proposed device. Note that the fabrication processes of the proposed structure are similar to those of a CSWC, making fabrication of the proposed PBS comparatively simple.

For different polarizations, the SWG offers an extra degree of freedom according to the effective-medium theory (EMT)[31] to design the material anisotropy by adjusting its duty cycle, material constituents, and grating profile (see the "Methods" section). Besides, the coupling length of a coupled waveguide is determined by using the formula of $L_i = \lambda/[2(n_{i,\,sym} - n_{i,\,aym})]$ in coupled mode theory[32], where *i* is the TE or TM, and $n_{i,sym}$ and $n_{i,asym}$ are the effective indices of the symmetrical and anti-symmetrical modes of the *i* mode, respectively. Before addressing the propagation properties of the proposed PBS, we first analyze its mode characteristics and coupling strengths. In this work, COMSOL Multiphysics software employing a rigorous finite element method was used to calculate the simulation results. The refractive indices of Si and SiO_2 at wavelength $\lambda = 1{,}550$ nm were $n_{Si} = 3.480$ and $n_{SiO2} = 1.444$[33], respectively. The geometry parameters selected were as follows: $h_{Si} = 150$ nm; $W_{cl} = 75$ nm; $g = 50$ nm; $\rho = 0.6$; $W_{Si} = 400$ nm; and $s = 550$ nm. Figure 3a shows the coupling length of the TM mode (L_{TM}) versus slot thickness, t_{slot}, for the proposed and CSWC structures. We observe that L_{TM} dramatically reduces as t_{slot} increases from 0 to 60 nm. Further increasing t_{slot}, the L_{TM} varies slightly. This is because a thicker t_{slot} leads to looser mode confinement, increasing the mode coupling strength. We know that the length of a PBS device is determined by the shorter mode coupling length. In the proposed structure, L_{TM} is much shorter than L_{TE}. Therefore, the TM mode is designed to be coupled to the cross bar, while the TE mode propagates along the through bar. Our numerical results show that the values of L_{TM} at $t_{slot} = 0$ (i.e., two Si strips without a slot layer[12]) and 55 nm are around 137 and 34 μm, respectively, for the CSWC[14]. In contrast, the L_{TM} at $t_{slot} = 55$ nm for the proposed PBS is only 9.9 μm long; a 70% reduction in device length compared to the CSWC, making the footprint of the proposed PBS ultra-compact. To evaluate the PER and IL of the PBS, another essential index, L_{TE} / L_{TM}, referred to as the coupling-length ratio of TE to TM modes, is shown in Fig. 3b.

A larger L_{TE} / L_{TM} means that less TE power couples to the cross channel (i.e., more TE power is preserved in the through channel), obtaining higher PER_{TM} and lower IL_{TE} (see the definitions of PER and IL in the "Methods" section). For the CSWC and our proposed structure, the maxima of L_{TE}/L_{TM} are 10.6 and 15,336 (three orders of magnitude higher), respectively, at $t_{slot} = 55$ nm. Remarkably, a non-trivial regime where $n_{sym} < n_{asym}$ for the TE mode (light yellow region in Fig. 3b) appears in our structure but not in the CSWC. Moving from a trivial coupling regime where $n_{sym} > n_{asym}$ to a non-trivial coupling regime where $n_{sym} < n_{asym}$, there is a transition point

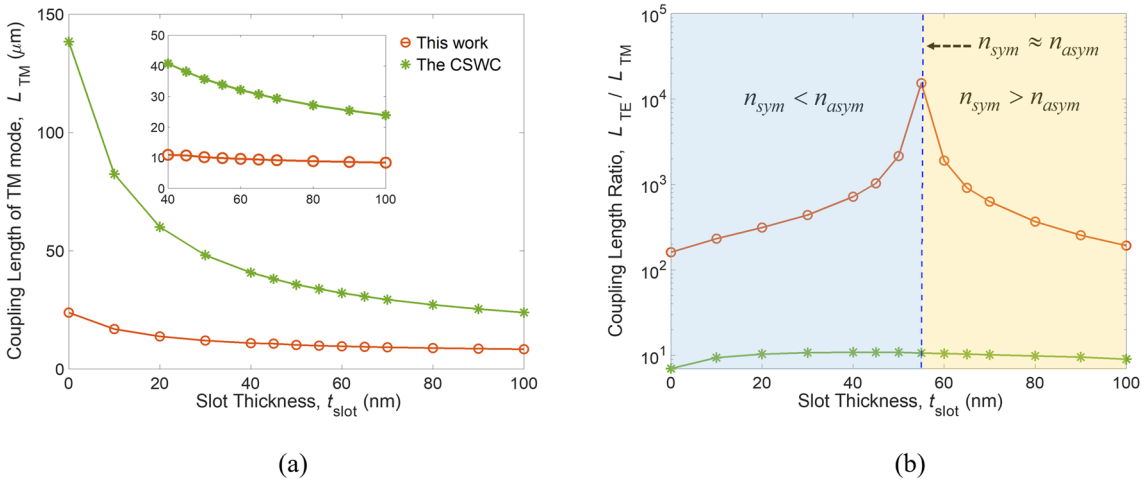

Figure 3. (**a**) Coupling lengths of TM (L_{TM}) and TE (L_{TE}) modes, and (**b**) the coupling-length ratio L_{TE}/L_{TM} as a function of slot thickness t_{slot} for the CSWC and the present design.

at $t_{slot} \approx 55$ nm where $n_{sym} \approx n_{asym}$, such that the coupling length of the TE mode approaches infinity, i.e., TE mode crosstalk is almost completely suppressed. As a result, selecting $t_{slot} = 55$ nm can achieve lowest coupling of the TE mode to the cross bar, thus significantly improving PER_{TM}.

The exceptionally low waveguide crosstalk can be explained by the presence of the SWGs[26]. Theoretically, mode confinement is determined by the refractive index contrast of the core and cladding. Therefore, TE mode coupling strength should increase if we replace the air cladding in the CSWC with anisotropic SWGs. However, the results obtained are counterintuitive. This can be understood by that the decay rate of the evanescent wave of the TE mode, k_{TE}, is determined by the ratio $\sqrt{\varepsilon_z/\varepsilon_x}$[26], and the condition $\varepsilon_z\,(=\varepsilon_y) > \varepsilon_x$ is always fulfilled according to Eqs. (2) and (3). For an isotropic cladding ($\varepsilon_z = \varepsilon_x$), k_{TE} is smaller than that of an anisotropic cladding, resulting in a longer evanescent tail for the TE mode. For the TM mode, the decay rate of its evanescent wave, k_{TM}, depends on $\sqrt{\varepsilon_z/\varepsilon_y} = 1$, making the confinement of TM mode is not affected by the anisotropic SWSWGs but is determined by the averaged permittivity of the SWSWG structure. The large permittivity of the cladding leads to looser TM mode confinement, thus increasing coupling between the two slot waveguides. In addition, the underlying mechanism of the transition point can be attributed to the anisotropic cladding of the SWSWGs causing the coupling coefficient of the TE mode to approach zero. To demonstrate the above explanations, field contours with a normalized amplitude of from 0 to 1 for TE (E_x) and TM (E_y) symmetrical modes for the proposed SWSWGs are shown in Fig. 4a,b, respectively; those for the CSWC[14] are shown in Fig. 4c,d, respectively. Evidently, the field overlap between the two main waveguides is significantly suppressed (enhanced) for the TE (TM) mode, compared with those of the CSWC.

Propagation characteristics and geometry tolerance of the present device. After obtaining the coupling length, we study the propagation characteristics of the proposed PBS. With the parameters used in Fig. 4 and $R = 3$ μm, Poynting power evolutions for the TE and TM modes are shown in Fig. 5a,b, respectively, at the modified coupling length, $L_{cm} = 8.9$ μm ($L_{TM} = 9.9$ μm), and those for the CSWC with $L_{cm} = 32.2$ μm ($L_{TM} = 33.88$ μm) are shown in Fig. 5c,d, respectively. Here, the L_{cm} is optimized for performance from the coupling length of TM mode, L_{TM}. As shown in Fig. 1a, a bent waveguide is connected at the end of the through channel to decouple the two modes. We moderately shorten the L_{TM} to be L_{cm} because the coupling remains for a short distance around 1 μm within the bent waveguide. The proposed PBS achieves $PER_{TE} = 24.13$ dB and $PER_{TM} = 26.02$ dB, and $IL_{TE} = 0.02$ dB and $IL_{TM} = 0.18$ dB. In contrast, the CSWS achieves $PER_{TE} = 23.13$ dB and $PER_{TM} = 13.55$ dB, and $IL_{TE} = 0.17$ dB and $IL_{TM} = 0.04$ dB.

Furthermore, PERs and ILs versus wavelength are shown in Fig. 6a,b, respectively, to evaluate the working BW of the PBS. We observe that PER_{TE} depends significantly on wavelength due to the short L_{TM}. By contrast, PER_{TM} shows slight variation on wavelength due to the extremely long $L_{TE} = 151.3$ mm. Within a BW of ~ 100 nm from $\lambda = 1{,}500$ to 1,600 nm, the PER_{TM} (PER_{TE}) of our device is greater than that of the CSWS by around 13 (3) dB. The proposed PBS achieves performance of $PER_{TM} > 25$ dB, $PER_{TE} > 20$ dB, $IL_{TE} < 0.05$ dB, and $IL_{TM} < 0.3$ dB within a BW of ~ 50 nm from $\lambda = 1{,}530$ to 1,580 nm. However, the PER_{TM} of the CSWC is less than 15 dB in the BW from $\lambda = 1{,}500$ to 1,600 nm. In fact, the $IL_{TE} < 0.05$ dB of the proposed structure extends to the entire band of 100 nm due to the transition point of $t_{slot} = 55$ nm being selected.

Theoretically, SWG structure exerts different effects on the propagation constants of symmetric and asymmetric modes with different field distributions, making the mode dispersion can be tailored by adjusting the geometry of SWG structure to reduce the wavelength sensitivity[23]. To demonstrate the expansion of the operating bandwidth of the present design, the relative variation of coupling length normalized by the coupling length ratio (i.e., $(\Delta L_\pi/L_\pi)/(L_{TE(TM)}/L_{TM})$ reflecting wavelength sensitivity) versus the wavelength is shown in Fig. 7. The reason of normalizing $\Delta L_\pi/L_\pi$ by the coupling length ratio is that the performances (see Fig. 6) are computed at the L_{TM} (i.e., device length) of $\lambda = 1.55$ μm. Therefore, $\Delta L_\pi/L_\pi$ reflects the wavelength sensitivity only for the TM mode (the coupling length ratio chosen here is $L_{TM}/L_{TM} = 1$) not for the TE mode (the coupling length ratio is

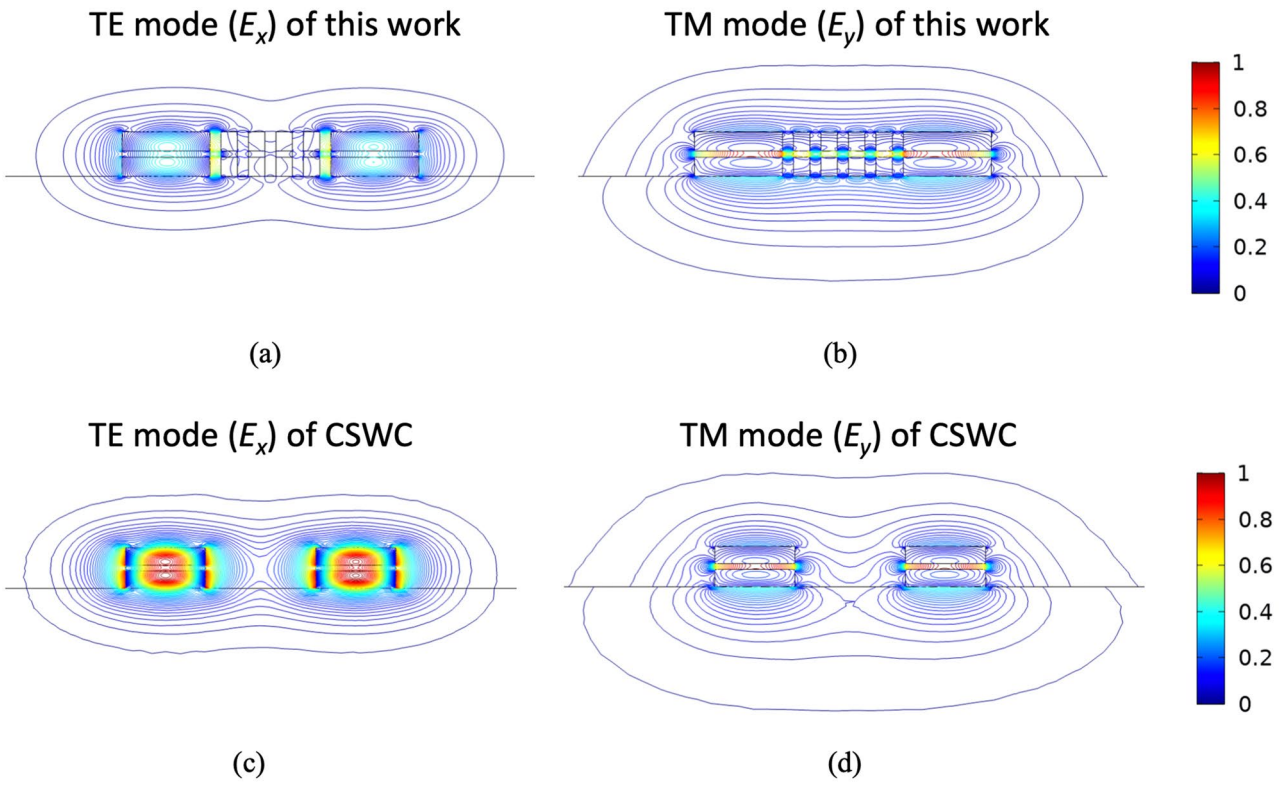

Figure 4. Field profiles of (**a**) TE and (**b**) TM symmetrical modes of the present design, and those of (**c**) TE and (**d**) TM ones of the CSWC[14], for $t_{slot} = 55$ nm, $W_{Si} = 400$ nm, $h_{Si} = 150$ nm, $W_{cl} = 75$ nm, $g = 50$ nm, and $s = 550$ nm.

L_{TE}/L_{TM}). The extremely slight wavelength sensitivity of the TE mode of this work demonstrates the high PER_{TM} as shown in Fig. 6. By contrast, the wavelength sensitivity of the TM mode shows moderate variation of PER_{TE}. We observe that the wavelength sensitivities of TE and TM modes of this work are smaller than those of the CSWC from $\lambda = 1.5$ to 1.6 μm, confirming the larger operation bandwidth than that of conventional DC-based PBSs.

To analyze the performance on device geometry, PERs and ILs versus t_{slot} are shown in Fig. 8a. It appears that the IL_{TE} is minimal and PER_{TM} is maximal at $t_{slot} = 55$ nm due to the maximum $L_{TE,}$ as predicted in "Results and discussion". Superior performance can be observed within the range $t_{slot} = 40$–70 nm. As mentioned above, a thicker t_{slot} leads to looser mode confinement, lengthening the coupling of the TM mode, L_{TM} (also L_{cm}), as shown in Fig. 8b. At the values of $t_{slot} = 10$ and 55 nm, the longest $L_{cm} = 14.5$ μm and shortest $L_{cm} = 7.6$ μm, respectively, are obtained. The dependence of h_{Si} on PERs and ILs is shown in Fig. 9a at $t_{slot} = 55$ nm. Excepting IL_{TM}, PER_{TE}, PER_{TM}, and IL_{TE} show slight variation over the range $h_{Si} = 120$ nm to 180 nm with $L_{cm} = 6.9$ to 12.4 μm, respectively, as shown in Fig. 9b.

As h_{Si} decreases, the TM mode shows looser confinement, resulting in higher IL_{TM}. This is because a significantly higher ratio of TM power is distributed to the SiO_2 substrate when h_{Si} is smaller than 140 nm. As a result, choosing the condition of $h_{Si} > 150$ nm preserves low TM mode loss. Considering the geometry variations of SWSWGs, PERs and ILs as a function of duty cycle ρ are shown in Fig. 10. After $\rho > 0.5$, the ILs of both modes increase significantly as ρ increases. This is attributed to weaker confinement of the TE and TM mode profiles. For the TE mode, this leads to more radiation loss while propagating through the curved waveguide. In contrast, greater power loss results from coupling of the TM mode into the cross bar. The L_{cm} significantly varies from 21.5 to 5.4 μm for $\rho = 0.2$ to $\rho = 0.8$, respectively, as shown in Fig. 10b. In experimental possibility, selecting a value close to $\rho = 0.5$ can effectively alleviate fabrication difficulties. Therefore, the trade-off between performance, footprint, and fabrication difficulty is to choose $\rho = 0.6$ with $L_{cm} = 8.9$ μm, rather than $\rho = 0.5$ with $L_{cm} = 11.3$ μm.

In addition to the duty cycle, we also investigated PERs and ILs versus number of strips, as shown in Fig. 11.

It is known that the scattering loss increases as the number of strips increases, resulting in a significantly higher ILs. However, PERs increases moderately with the increase in number of strips. This is because although the loss of major power decreases for each bar, PER is dominated by the reduction of the other minor power, making the PER increase moderately. Notice that the device length is almost invariant with increasing number of strips. Finally, we evaluated fabrication tolerance of the proposed PBS. The PERs and ILs versus the variations of slot thickness, Δt_{slot}, thickness of Si layer, Δh_{Si}, and width of SWSWGs, ΔW_{cl} are shown in Fig. 12a–c, respectively. For Δt_{slot} and Δh_{Si}, PER_{TE} and PER_{TM} achieve > 20 dB and IL_{TE}, and IL_{TM} are < 0.3 dB for the variations in Δt_{slot} and Δh_{Si} within ± 10 nm. Thanks to the present experimental technology, the surface roughness of thin film depositions for SiO_2 and Si layers is smaller than 5 nm using widely used plasma-enhanced chemical vapor deposition[34].

For ΔW_{cl}, PER_{TE} and IL_{TM} vary significantly because of the short L_{TM}, resulting in a large deviation from the PMC. By contrast, PER_{TM} and IL_{TE} are slight variation due to the almost infinite long coupling length (achieving

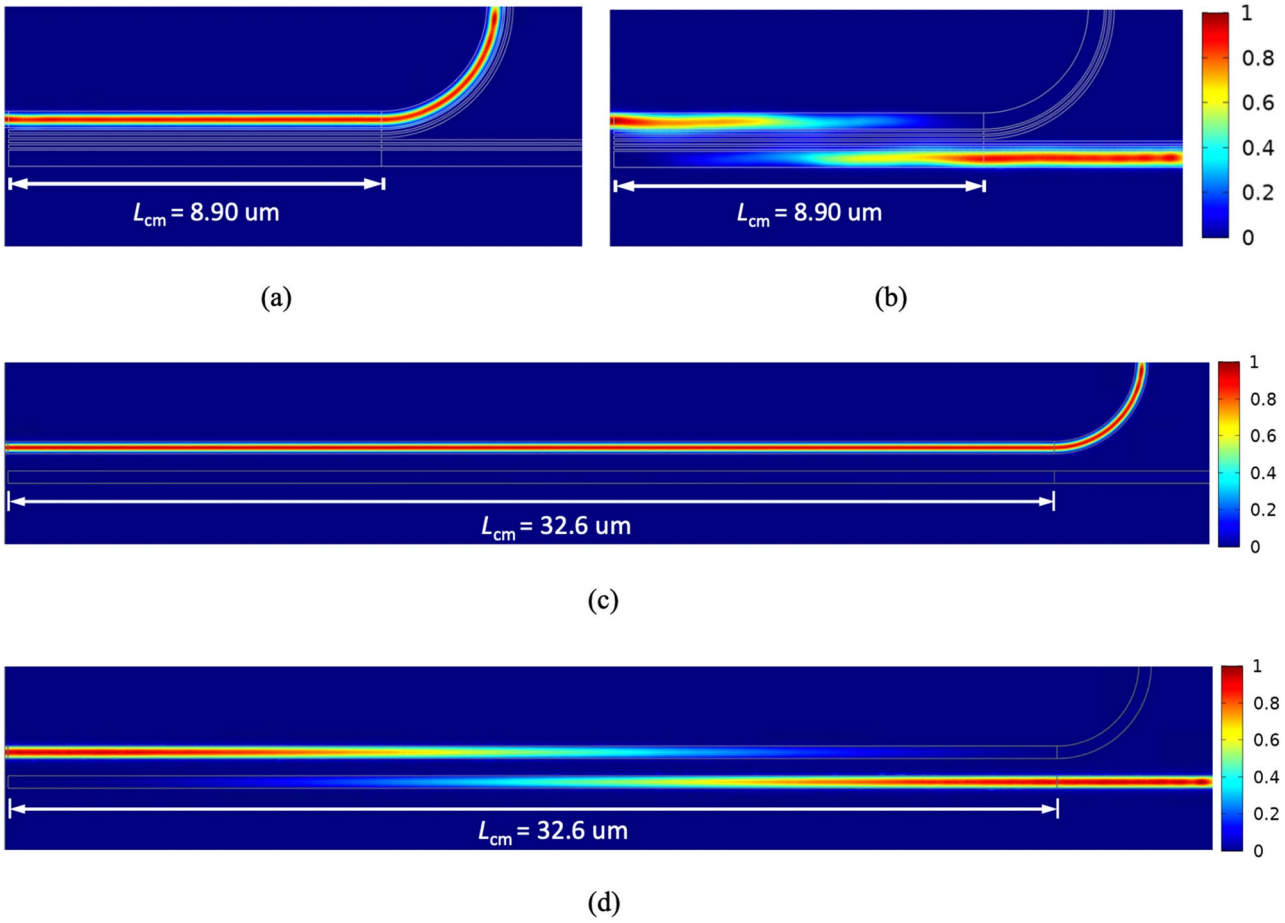

Figure 5. Poynting power evolutions for the (**a**) TE and (**b**) TM modes of the proposed PBS with $L_{TM} = 9.91$ μm ($L_{cm} = 8.9$ μm), and those of the (**c**) TE and (**d**) TM modes of the CSWC with $L_{TM} = 33.88$ μm ($L_{cm} = 32.6$ μm).

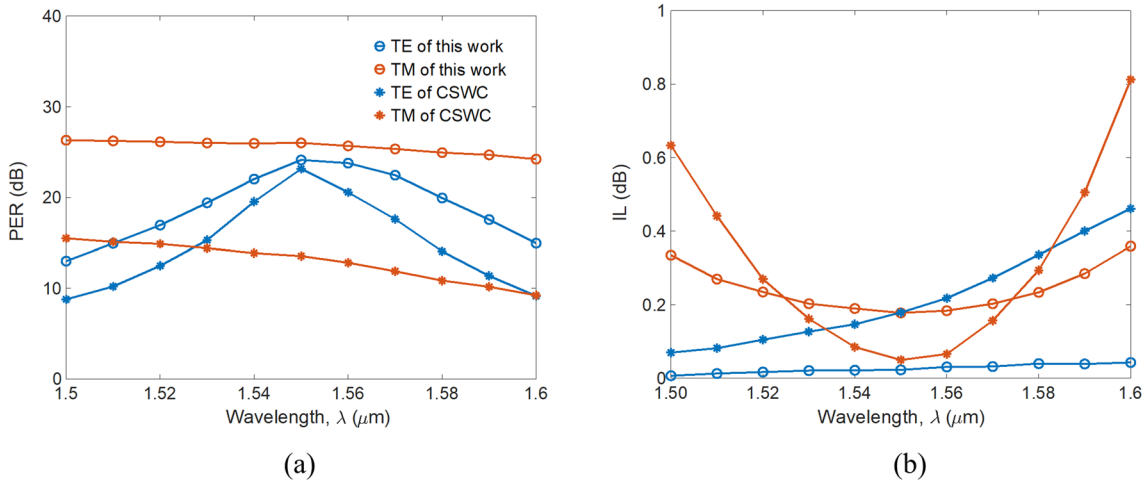

Figure 6. (**a**) PER and (**b**) IL as a function of wavelength with $t_{slot} = 55$ nm for the present structure and the CSWC.

almost zero crosstalk) of the TE mode ($L_{TE} = 151.3$ mm at the transition point of $t_{slot} = 55$ nm, $W_{cl} = 75$ nm, and $h_{Si} = 150$ nm). For the condition of $\Delta W_{cl} < 5$ nm, $PER_{TE} > 20$ dB, $PER_{TM} > 25$ dB, $IL_{TM} < 0.06$ dB, and $IL_{TM} < 0.3$ dB. From the calculated results, the most critical geometry affecting performance is the width of SWSWG. Fortunately, a mixed inductively coupled plasma-reactive ion etching process and hydrogen annealing[35] can achieve sidewall roughness of a Si strip to < 1 nm.

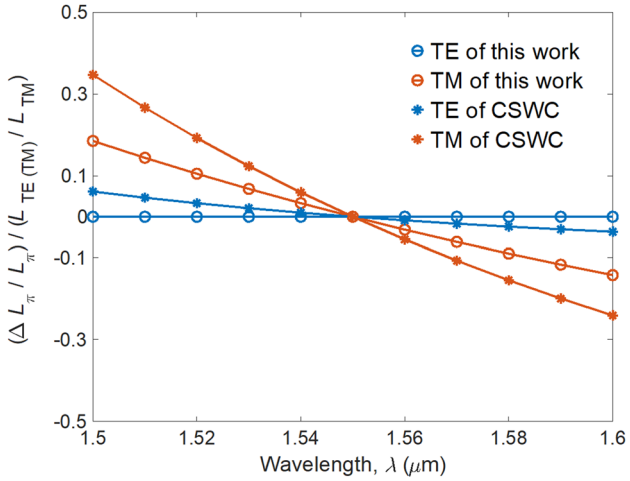

Figure 7. Wavelength sensitivity $(\Delta L_\pi/L_\pi)/(L_{TE(TM)}/L_{TM})$ as a function of wavelength for the present structure and the CSWC.

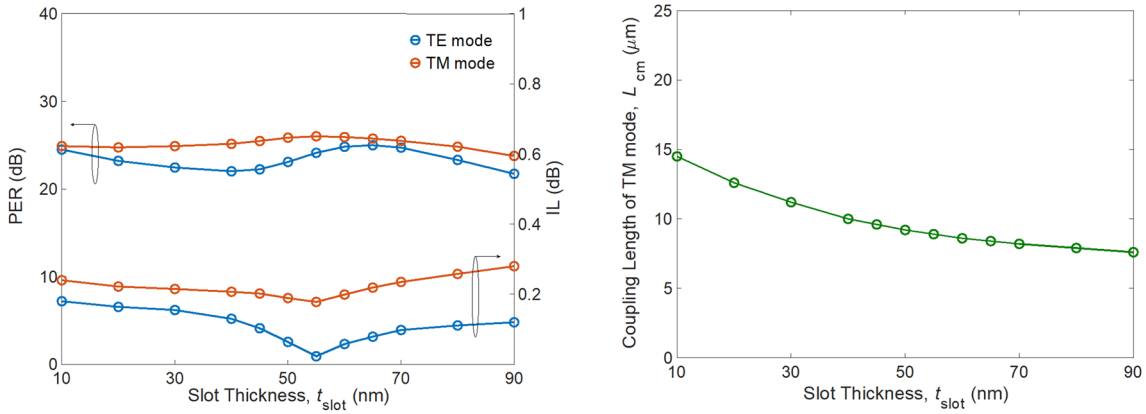

Figure 8. (**a**) PER (left axis) and IL (right axis), and (**b**) modified coupling length of the TM mode L_{cm} as a function of slot thickness t_{slot}.

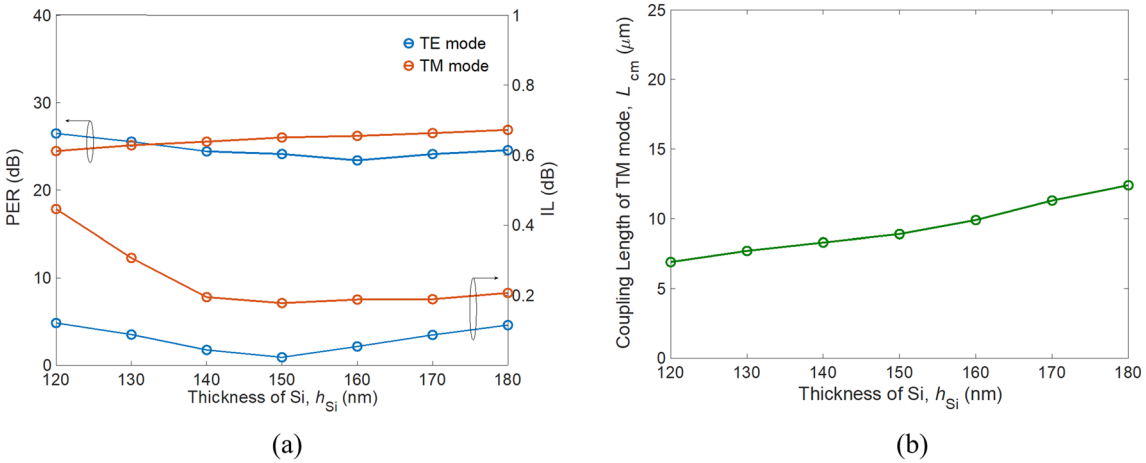

Figure 9. (**a**) PER (left axis) and IL (right axis), and (**b**) modified coupling length of TM mode L_{cm} as a function of Si thickness h_{Si}.

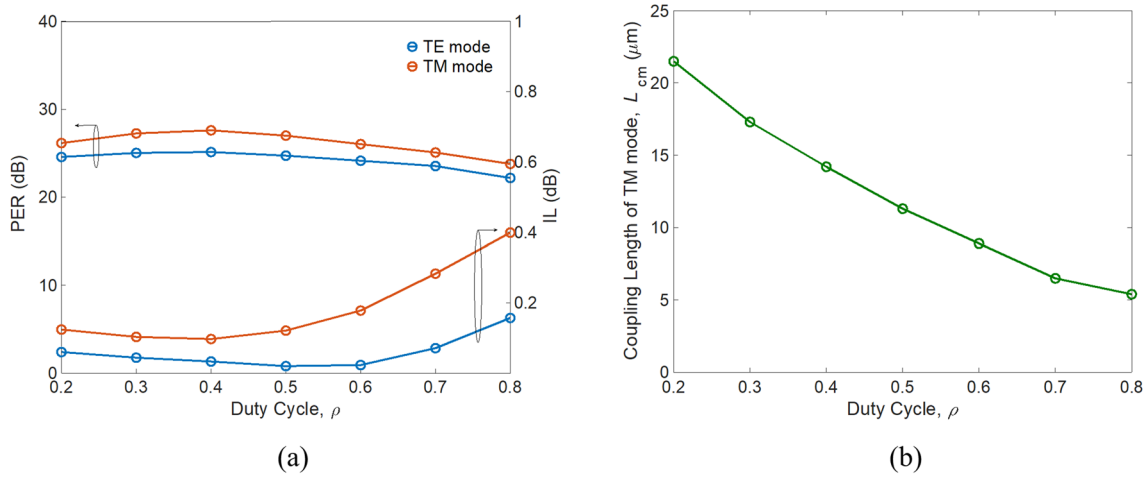

Figure 10. (**a**) PER (left axis) and IL (right axis), and (**b**) modified coupling length of TM mode L_{cm} as a function of duty cycle ρ.

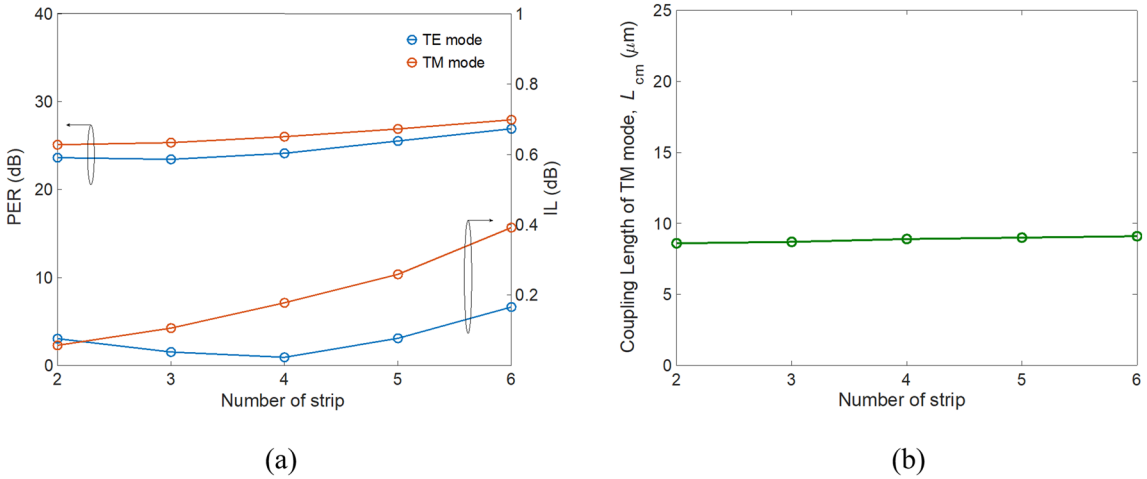

Figure 11. (**a**) PER (left axis) and IL (right axis), and (**b**) modified coupling length of TM mode L_{cm} as a function of number of strips.

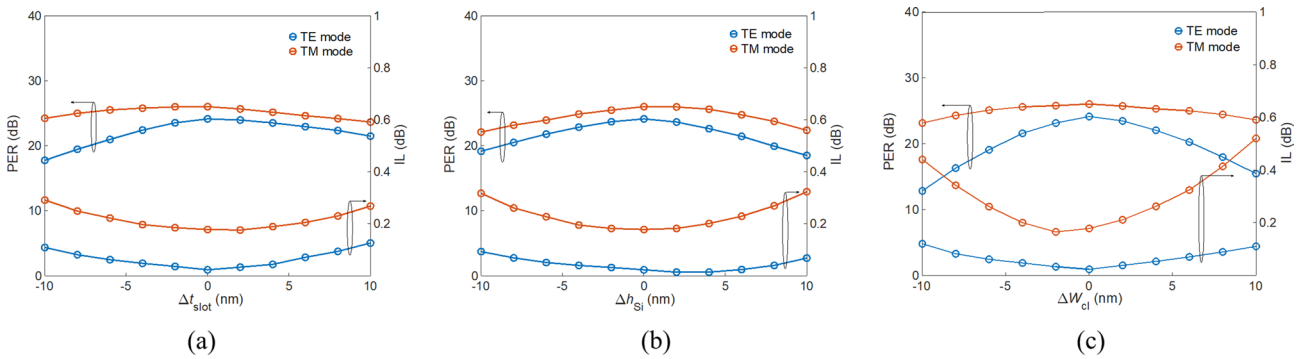

Figure 12. PER (left axis) and IL (right axis) as functions of variation in (**a**) slot thickness Δt_{slot}, (**b**) thickness of Si Δh_{Si}, and (**c**) width of SWSWGs ΔW_{cl}.

In conclusion, we propose an ultra-compact, high-performance PBS, consisting of slotted waveguides with SWSWGs. By controlling the optical momentum of evanescent waves with the anisotropic SWSWGs, the coupling strength of the TE mode is suppressed remarkably, and that of TM mode is significantly enhanced. As a result, the proposed PBS significantly improves the PER of the TM mode by around 13 dB and reduces device length by > 70% (from 32.2 to 8.9 μm), when compared with a CSWC that does not include SWSWGs. Extraordinarily,

the transition point of $n_{sym} \approx n_{asym}$ found in this work almost entirely eliminates TE mode crosstalk between the waveguides. This interesting phenomenon could be applied to building highly dense PICs and will be studied in depth elsewhere. In terms of practical fabrication, the required steps were identical to those of a CWSC, making fabrication of the proposed PBS comparatively simple. Our numerical simulations demonstrate that the proposed PBS achieves $PER_{TM} > 25$ dB, $PER_{TE} > 20$ dB, $IL_{TE} < 0.05$ dB, and $IL_{TM} < 0.3$ dB within a BW of ~ 50 nm from λ = 1,530 to 1,580 nm. In terms of fabrication tolerance, PER_{TE} and PER_{TM} achieve > 20 dB, and IL_{TE} and IL_{TM} are < 0.3 dB for variations in slot thickness and Si thickness within ± 10 nm. These calculated results show that the critical geometry is SWSWG width.

Methods

According to the effective-medium theory (EMT)[31], which limits the grating pitch Λ to a smaller than subwavelength scale, the SWG regions demonstrate equivalent material anisotropy as follows:

$$\varepsilon_{EMT} = \begin{bmatrix} \varepsilon_x & 0 & 0 \\ 0 & \varepsilon_y & 0 \\ 0 & 0 & \varepsilon_z \end{bmatrix}, \tag{1}$$

$$\varepsilon_y = \varepsilon_z = \rho\,\varepsilon_H + (1-\rho)\varepsilon_L, \tag{2}$$

$$\varepsilon_x^{-1} = \rho\varepsilon_H^{-1} + (1-\rho)\varepsilon_L^{-1}, \tag{3}$$

where ε_x, ε_y, and ε_z are the equivalent permittivities in the x-, y-, and z-directions, respectively, and ε_H (here ε_{Si}) and ε_L (here ε_{air}) are the high and low permittivities of the SWG. Additionally, the PER and IL of the two modes are defined in Eqs. (4) and (5), respectively[15]:

$$\mathrm{PER}_{TE(TM)} = 10\ \log_{10}\left(\frac{P_{TE(TM),\,thr(cross)}}{P_{TM(TE),\,thr(cross)}}\right), \tag{4}$$

$$\mathrm{IL}_{TE(TM)} = -10\ \log_{10}\left(\frac{P_{TE(TM),\,thr(cross)}}{P_{input}}\right), \tag{5}$$

where P_{input} is the input power, $P_{TE(TM),\,thr(cross)}$ is the TE (TM) mode power at the through (cross) channel, and $P_{TM(TE),\,thr\,(cross)}$ is the TM (TE) mode power at the through (cross) channel.

Received: 30 May 2020; Accepted: 14 July 2020
Published online: 30 July 2020

References

1. Rahim, A., Spuesens, T., Baets, R. & Bogaerts, W. Open-access silicon photonics: current status and emerging initiatives. *Proc. IEEE* **106**, 2313–2330 (2018).
2. Bogaerts, W. & Chrostowski, L. Silicon photonics circuit design: method, tools, and challenges. *Laser Photon. Rev.* **12**, 1700237 (2018).
3. Dai, D., Bauters, J. & Bowers, J. E. Passive technologies for future large-scale photonic integrated circuits on silicon: polarization handling, light non-reciprocity and loss reduction. *Light-Sci. Appl.* **1**, e1 (2012).
4. Gao, L., Huo, Y., Harris, J. S. & Zhou, Z. Ultra-compact and low-loss polarization rotator based on asymmetric hybrid plasmonic waveguide. *IEEE Photon. Technol. Lett.* **25**, 2081–2084 (2013).
5. Xu, H. & Shi, Y. Ultra-compact and highly efficient polarization rotator utilizing multi-mode waveguides. *Opt. Lett.* **42**, 771–774 (2017).
6. Watts, M. R., Haus, H. A. & Ippen, E. P. Integrated mode-evolution-based polarization splitter. *Opt. Lett.* **30**, 967–969 (2005).
7. Hong, J. M. *et al.* Design and fabrication of a significantly shortened multimode interference coupler for polarization splitter application. *IEEE Photon. Technol. Lett.* **15**, 72–74 (2003).
8. Han, L. S., Liang, S., Zhu, H. L., Zhang, C. & Wang, W. A High extinction ratio polarization beam splitter with MMI couplers on InP substrate. *IEEE Photon. Technol. Lett.* **27**, 782–785 (2015).
9. Feng, J. & Zhou, Z. Polarization beam splitter using a binary blazed grating coupler. *Opt. Lett.* **32**, 1662–1664 (2007).
10. Tang, Y. B., Dai, D. & He, S. Proposal for a grating waveguide serving as both a polarization splitter and an efficient coupler for silicon-on-insulator nanophotonic circuits. *IEEE Photon. Technol. Lett.* **21**, 242–244 (2009).
11. Shen, B., Wang, P., Polson, R. & Menon, R. An integrated-nanophotonics polarization beamsplitter with 2.4 × 2.4 μm2 footprint. *Nat. Photon.* **9**, 378–382 (2015).
12. Fukuda, H. *et al.* Ultrasmall polarization splitter based on silicon wire waveguides. *Opt. Express* **14**, 12401–12408 (2013).
13. Guan, X., Wu, H., Shi, Y., Wosinski, L. & Dai, D. Ultracompact and broadband polarization beam splitter utilizing the evanescent coupling between a hybrid plasmonic waveguide and a silicon nanowire. *Opt. Lett.* **38**, 3005–3008 (2013).
14. Yue, Y., Zhang, L., Yang, J. Y., Beausoleil, R. G. & Willner, A. E. Silicon-on-insulator splitter using two horizontally slotted waveguides. *Opt. Lett.* **35**, 1364–1366 (2010).
15. Zhang, H. *et al.* Polarization splitter using horizontal slot waveguide. *Opt. Express* **21**, 3363–3369 (2013).
16. Almeida, V. R., Xu, Q., Barrios, C. A. & Lipson, M. Guiding and confining light in void nanostructure. *Opt. Lett.* **29**, 1209–1211 (2004).
17. Xu, Q., Almeida, V. R., Panepucci, R. R. & Lipson, M. Experimental demonstration of guiding and confining light in nanometer-size low-refractive-index material. *Opt. Lett.* **29**, 1626–1628 (2004).
18. Halir, R. *et al.* Subwavelength-grating metamaterial structures for silicon photonic devices. *Proc. IEEE* **106**, 2144–2156 (2018).
19. Cheben, P., Halir, R., Schmid, J. H., Atwater, H. A. & Smith, D. R. Subwavelength integrated photonics. *Nature* **560**, 565–572 (2018).
20. Halir, R., Cheben, P., Luque-González, J. M., Sarmiento-Merenguel, J. D. & Schmid, J. H. Ultra-broadband nanophotonic beamsplitter using an anisotropic sub-wavelength metamaterial. *Laser Photon. Rev.* **10**, 1039–1046 (2016).

21. Xu, Y. & Xiao, J. Compact and high extinction ratio polarization beam splitter using subwavelength grating couplers. *Opt. Lett.* **41**, 773–776 (2016).
22. Liu, L., Deng, Q. & Zhou, Z. Manipulation of beat length and wavelength dependence of a polarization beam splitter using a subwavelength grating. *Opt. Lett.* **41**, 5126–5129 (2016).
23. Halir, R. *et al.* Waveguide sub-wavelength structures: a review of principles and applications. *Laser Photon. Rev.* **9**, 25–49 (2015).
24. Xiong, Y. *et al.* Polarization splitter and rotator with subwavelength grating for enhanced fabrication tolerance. *Opt. Lett.* **39**, 6931–6934 (2014).
25. Halir, R. *et al.* Colorless directional coupler with dispersion engineered sub-wavelength structure. *Opt. Express* **20**, 13470–13477 (2012).
26. Jahani, S. & Jacob, Z. Transparent subdiffraction optics: nanoscale light confinement without metal. *Optica* **1**, 96–100 (2014).
27. Jahani, S. & Jacob, Z. Photonic skin-depth engineering. *J. Opt. Soc. Am. B* **32**, 1346–1353 (2015).
28. Jahani, S. *et al.* Controlling evanescent waves using silicon photonic all-dielectric metamaterials for dense integration. *Nat. Commun.* **9**, 1893 (2018).
29. Xu, H., Dai, D. & Shi, Y. Ultra-broadband and ultra-compact on-chip silicon polarization beam splitter by using hetero-anisotropic metamaterials. *Laser Photon. Rev.* **13**, 1800349 (2019).
30. Li, C., Dai, D., Bowers, J. E. Ultra-broadband and low-loss polarization beam splitter on silicon. *Optical Fiber Communication Conference (OFC), OSA Technical Digest (Optical Society of America)*, paper Th1A.4 (2020).
31. Lalanne, P., Astilean, S., Chavel, P., Cambril, E. & Launois, H. Design and fabrication of blazed binary diffractive elements with sampling periods smaller than the structure cutoff. *J. Opt. Soc. Am. A* **16**, 1346–1353 (1999).
32. Yariv, A. & Yeh, P. *Optical waves in crystals: propagation and control of laser radiation* (Wiley-Interscience, NJ, USA, 2002).
33. Bass, M. Handbook of optics, Third Edition Volume IV: optical properties of materials, nonlinear optics, quantum optics. (McGraw-Hill Education, NJ, USA, 2009).
34. Amirzada, M. R., Tatzel, A., Viereck, V. & Hillmer, H. Surface roughness analysis of SiO_2 for PECVD, PVD and IBD on different substrates. *Appl. Nanosci.* **6**, 215–222 (2016).
35. Gao, F., Wang, Y., Cao, G., Jia, X. & Zhang, F. Reduction of sidewall roughness in silicon-on-insulator rib waveguides. *Appl. Surf. Sci.* **252**, 5071–5075 (2006).

Acknowledgements

The authors would like to thank the National Science Council of the Republic of China, Taiwan for financially supporting this research under Contract No. MOST 108-2112-M-005-006. The authors would like to thank Enago (https://www.enago.tw) for the English language review.

Author contributions

All authors conceived the designed idea and discussed the results. C.-C.H. performed the numerical simulations. C.-C.H. wrote the manuscript and supervised the whole work.

Competing interests

The author declares no competing interests.

Additional information

Correspondence and requests for materials should be addressed to C.-C.H.

Reprints and permissions information is available at www.nature.com/reprints.

Publisher's note Springer Nature remains neutral with regard to jurisdictional claims in published maps and institutional affiliations.